PAPER • OPEN ACCESS

Effects of multiple elastic and inelastic scattering on energy-resolved contrast in Kikuchi diffraction

New Journal of Physics
The open access journal at the forefront of physics

Deutsche Physikalische Gesellschaft DPG
IOP Institute of Physics

Published in partnership with: Deutsche Physikalische Gesellschaft and the Institute of Physics

OPEN ACCESS

RECEIVED
21 August 2019

REVISED
3 November 2019

ACCEPTED FOR PUBLICATION
28 November 2019

PUBLISHED
13 December 2019

PAPER

Effects of multiple elastic and inelastic scattering on energy-resolved contrast in Kikuchi diffraction

M Vos[1] **and A Winkelmann**[2,3]

[1] Electronic Materials Engineering, Research School of Physics, Australian National University, Canberra, ACT, Australia
[2] Laser Zentrum Hannover e.V., D-30419 Hannover, Germany
[3] Academic Centre for Materials and Nanotechnology, AGH University of Science and Technology, al. A. Mickiewicza 30, 30-059 Krakow, Poland

E-mail: maarten.vos@anu.edu.au

Keywords: electron energy loss, silicon, Kikuchi pattern

Abstract

Energy-resolved Kikuchi patterns for silicon crystals were measured for 30 keV electrons in a reflection geometry. The amount of contrast seen depends strongly on both the geometry and the energy loss. For geometries where the outgoing trajectory is glancing with the surface, the contrast is maximum for zero loss, decreases with larger energy losses and for energy losses over 1 keV, a reversal of the contrast is observed. For geometries where the incoming beam is glancing, the contrast first gradually increases with energy loss and decreases slowly for losses larger than 100 eV. Under these conditions contrast reversal was not seen. These observations are modelled using the cross sections of the various elastic and inelastic processes involved.

1. Introduction

Kikuchi diffraction [1] results from the coherent scattering of diffusely scattered electrons inside a crystal [2, 3]. In the scanning electron microscope (SEM), the technique of Electron backscatter diffraction (EBSD) relies on the Kikuchi mechanism to study crystal orientations and phase distributions of materials. In EBSD, Kikuchi diffraction patterns are commonly detected on a phosphor screen near the sample, at primary electron beam energies in the range from about 5 to 30 keV. The group of electrons which contributes to the observed Kikuchi pattern in EBSD, however, often constitutes only a minor portion of the signal (at most 10%–20%) relative to a dominating background intensity which does not show diffraction contrast. An extended energy range of the backscattered electron spectrum contributes to the observed EBSD signal and influences the formation of the observed diffraction effects. This is caused by the absence of any dedicated energy-filtering in a typical EBSD setup, where the electrons are detected by light emission from a phosphor screen. It is thus important to understand the different mechanisms of multiple elastic and inelastic scattering which lead to the specific weighting of Kikuchi diffraction relative to the background intensity.

As an example, we show a measured raw EBSD pattern of a silicon sample in figure 1, where the actual Kikuchi diffraction contribution is seen as a network of crossing bands with intensity higher than the background. These bands have an angular width of about twice the Bragg angle, and are centered along the projection of the reflecting lattice planes [3]. In figure 1 it is also clearly seen that the Kikuchi diffraction features reside on a smooth background which includes in the order of 90% of the total intensity.

The Kikuchi patterns observed in EBSD are formed when electrons emerge after scattering over large angles from atoms in a crystal, and, depending on the site of backscattering in the unit cell, the Kikuchi diffraction patterns can differ greatly [5]. In figure 2, we show several examples of the possible effects that lead to averaging out of the Kikuchi diffraction pattern. As can be seen in figure 2(a), if the electrons emerge from many different random sites in the unit cell, the diffraction pattern will tend to average out to a structureless distribution, as was discussed in detail in [6]. A special case of this effect are site-specific Kikuchi diffraction patterns, which are shown in figure 2(b) for the case of Rutile TiO_2 [7]. Here, electrons originating from oxygen sites can have dark bands where those originating from Ti sites have light bands, leading to a partial cancellation of diffraction

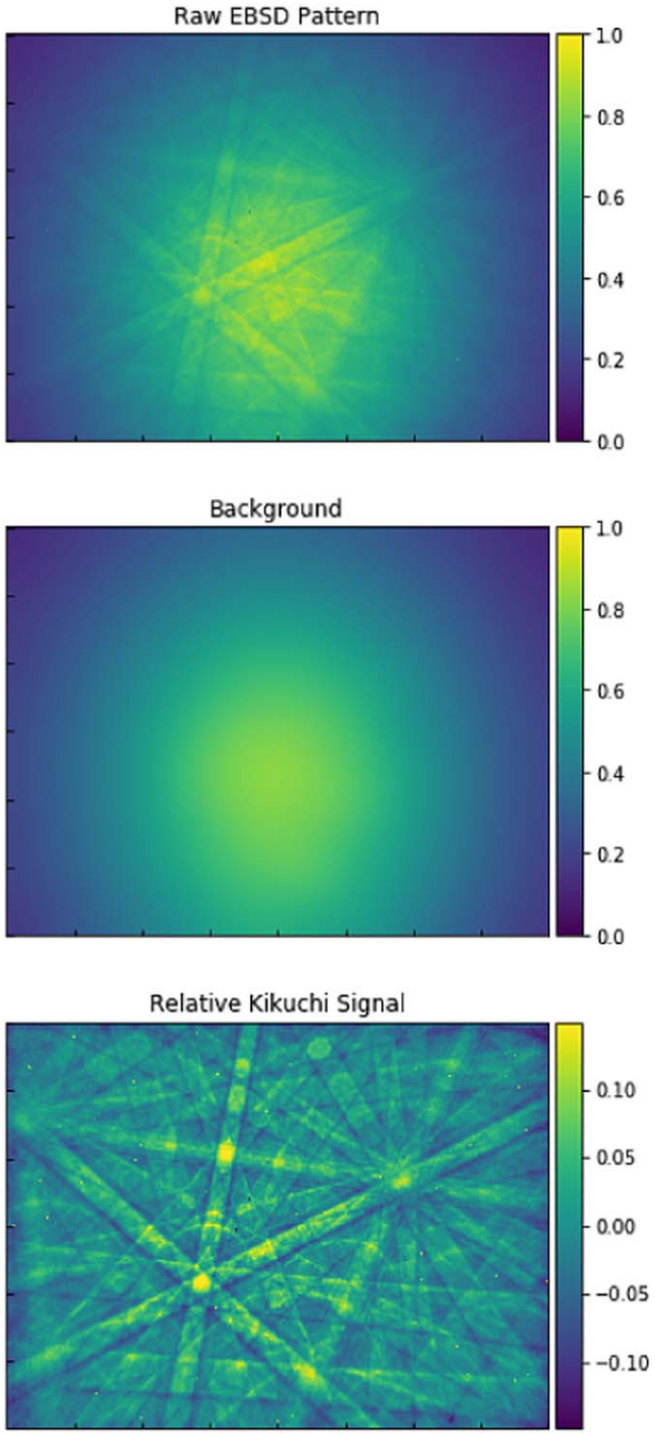

Figure 1. Top: Raw Si EBSD pattern collected at a primary beam energy of 15 keV. Center: background intensity obtained by low-pass FFT filtering. Bottom: Kikuchi signal relative to the background signal. For a discussion of quantitative image processing of EBSD patterns see [4].

contrast when the sum of both processes is observed. Another intriguing consequence of multiple incoherent interactions is the phenomenon of contrast reversal, i.e. Kikuchi bands can be observed with decreased or increased intensity relative to the background. Such contrast reversal effects can be observed in both transmission and reflection under specific conditions [2, 8–10].

The central question which will be addressed in this paper is: if we have no explicit energy filtering in EBSD and if, in principle, we can have all the different kinds of possible Kikuchi pattern contrast distributions shown in figure 2, why at all do we see a diffraction pattern in the backscattered electron distribution, and what is the relevant energy range contributing to the observed diffraction contrast? In order to answer this question, it is essential to know which elastic and inelastic collisions localize the scattered beam on a lattice site, and which not

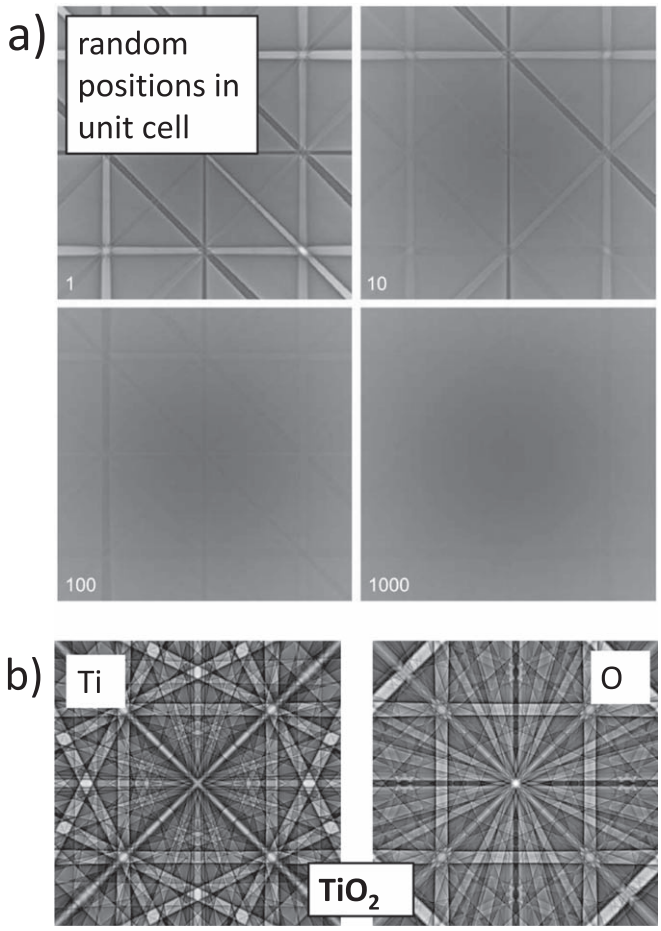

Figure 2. Possible contributions to Kikuchi patterns. (a) The calculated diffraction pattern considering a varying number of (randomly chosen) positions of the sources of electron in a unit cell as indicated. With an increasing number of sources, the diffraction pattern averages out and thus disappears. (From [6]) (b) calculated site-specific Kikuchi diffraction for Rutile TiO_2 as was also measured with a separation of the elements based on the recoil effect [7]. Note that the horizontal and vertical Kikuchi bands have opposite contrast for Ti and O and thus the Kikuchi contrast decreases when these intensities are summed.

and how frequently these collisions occur. As we will discuss below, the main types of scattering events which need to be considered are incoherent large-angle deflections from the target atomic cores, coherent small-angle deflections from these atoms, as well as inelastic scattering due to electronic excitations induced by the projectile electron. We will argue that Kikuchi pattern formation is controlled by the fact that the mean free path λ^{quasi} between quasi-elastic, incoherent, large-angle scattering events is about an order of magnitude larger than the inelastic mean free path λ^{in} for electronic losses. Qualitatively, this means that, compared to quasi-elastic events which create Kikuchi sources, inelastic events are relatively frequent and will strongly influence the contrast of Kikuchi patterns as a function of the energy loss. We will present experimental data which quantifies this statement by measurements of Kikuchi band contrast as a function of energy loss in a systematically varying scattering geometry. For the interpretation of our experimental data, we develop a qualitative model which explains the observed trends using only 4 key parameters. Our analysis will show that there is an implicit energy filtering in the Kikuchi diffraction process. A pronounced Kikuchi pattern contrast can be preserved only for a relatively low number of inelastic losses after the creation of a Kikuchi pattern source. In the limit of large energy losses, an increasing fraction of the scattered electrons at the respective energy will show no Kikuchi contrast and will contribute to the background signal only. Taking these findings into account, we will discuss possible implications of our results for Monte-Carlo simulations in the context of Kikuchi diffraction.

2. Elastic and inelastic electron scattering

In the following, we summarize the properties of *particle* scattering in a medium, emphasizing a picture of electron scattering at the atoms of the sample. These scattering processes are also relevant for Monte Carlo simulations of electron trajectories in electron spectroscopy and microanalysis. For the classical picture of particle scattering to be reconciled with experimental observations related to *wave*-like properties of electrons in

crystals, the consequences of the transfer of energy and momentum as a result of the scattering processes have to be considered. In a crystalline sample, the possible interference effects of the scattered electrons can be affected in characteristically different ways by energy losses and momentum changes.

2.1. Quasi-elastic mean free path

The elastic differential cross section $\left(\mathrm{DCS},\ \frac{\mathrm{d}\sigma}{\mathrm{d}\Omega}\right)$ for electrons scattering from a single atom over an angle θ can be calculated using the partial wave formalism [11]. It gives the probability that an electron scatters from a potential, defined by the atomic charge distribution, into a specific direction. The total elastic cross section $\sigma_{\mathrm{tot}}^{\mathrm{el}}$ can be calculated by integration over $\frac{\mathrm{d}\sigma}{\mathrm{d}\Omega}$:

$$\sigma_{\mathrm{tot}}^{\mathrm{el}} = \int_0^{\pi} \frac{\mathrm{d}\sigma}{\mathrm{d}\Omega} 2\pi \sin\theta \mathrm{d}\theta. \tag{1}$$

For an amorphous material with N atoms per unit volume this gives the elastic mean free path (MFP):

$$\lambda^{\mathrm{el}} = \frac{1}{N\sigma_{\mathrm{tot}}^{\mathrm{el}}}. \tag{2}$$

For a crystal, this picture needs to be modified. For small scattering angles, the scattering contributions emerging from different atoms add coherently and one has to consider diffraction.

In contrast to scattering from a potential, the case considered in a partial wave calculation, in reality the electron scatters from an atom with mass M_a. If the incoming electron with energy E_0 has a momentum $\boldsymbol{p}_0$ and is scattered over an angle θ, a momentum $\boldsymbol{q}$ is transferred to the atom with magnitude:

$$q(\theta) = 2p_0 \sin\left(\frac{\theta}{2}\right). \tag{3}$$

Assuming that the atom was stationary before the collision, it will acquire a kinetic energy $q^2/2M_a$. We will refer to this type of collisions as 'quasi-elastic'. Diffraction involves a coherent interaction in an extended region of the crystal with mass M_c (and thus $M_c/m_e \approx \infty$), and then the energy transfer is $q^2/2M_c \approx 0$, i.e. there is virtually no energy transfer to the crystal and the electron is scattered elastically. If the electron interacts quasi-elastically with a single atom in a crystal, then the recoil energy involved will lead to phonon excitations. For very large q values, this energy transfer can be measured experimentally [12] and can be used to identify the scattering element.

In diffraction processes in crystals, the excitation of phonons reduces coherence with respect to the incident beam [13], with a localization of the quasielastic scattering processes at atomic positions inside a crystal. In order to discriminate between the possibilities of coherent versus incoherent scattering in the elastic cross section of an atom in a crystal, one can use the Debye–Waller factor which describes the differential cross section for coherent scattering $\frac{\mathrm{d}\sigma}{\mathrm{d}\Omega}_{\mathrm{coh}}$ relative to the intensity $\frac{\mathrm{d}\sigma}{\mathrm{d}\Omega}_{0}$ without thermal vibrations:

$$\frac{\mathrm{d}\sigma}{\mathrm{d}\Omega}_{\mathrm{coh}}(q) = \frac{\mathrm{d}\sigma}{\mathrm{d}\Omega}_{0}(q)\, \mathrm{e}^{-q^2\langle u^2\rangle/3}, \tag{4}$$

where $\langle u^2\rangle$ is the mean square displacement of the atoms due to vibrations, including the zero point motion. Accordingly, the incoherent or quasi-elastic part of the scattered intensity is given by:

$$\frac{\mathrm{d}\sigma}{\mathrm{d}\Omega}_{\mathrm{quasi}}(q) = \frac{\mathrm{d}\sigma}{\mathrm{d}\Omega}_{0}(q)\, [1.0 - \mathrm{e}^{-q^2\langle u^2\rangle/3}], \tag{5}$$

For silicon at room temperature $\langle u^2\rangle = 0.0059\ \text{Å}^2$ [14]. If we consider the q-value for which the coherent intensity is reduced by a factor of 2 as the lower boundary of the large-angle regime, this corresponds to a momentum transfer of $q = 18.7\ \text{Å}^{-1}$ or 9.9 a.u. (atomic unit of momentum $= \hbar/a_0$). For 20 keV electrons, this leads to a characteristic scattering angle of $\theta_{1/2} = 14.7°$. For scattering angles larger than $\theta_{1/2}$, incoherent quasi-elastic scattering is more probable, while for lower angles, diffraction via coherent forward-scattering is dominant. We now assume that one can calculate the total cross section $\sigma_{\mathrm{tot}}^{\mathrm{quasi}}$ of quasi-elastic, incoherent scattering from an atom in a crystal by replacing the lower limit of the integration in equation (1) by $\theta_{1/2}$:

$$\sigma_{\mathrm{tot}}^{\mathrm{quasi}} = \int_{\theta_{1/2}}^{\pi} \frac{\mathrm{d}\sigma}{\mathrm{d}\Omega} 2\pi \sin\theta \mathrm{d}\theta. \tag{6}$$

An alternative way to define $\sigma_{\mathrm{tot}}^{\mathrm{quasi}}$ is to weight the cross section by the incoherent fraction, similarly as done by Wang [15] and Rossouw and Bursill [16] in the description of the mean free path for thermal diffuse scattering:

$$\sigma_{\mathrm{tot}}^{\mathrm{quasi}} = \int_0^{\pi} (1 - \mathrm{e}^{-q(\theta)^2\langle u^2\rangle^2/3}) \frac{\mathrm{d}\sigma}{\mathrm{d}\Omega} 2\pi \sin\theta \mathrm{d}\theta. \tag{7}$$

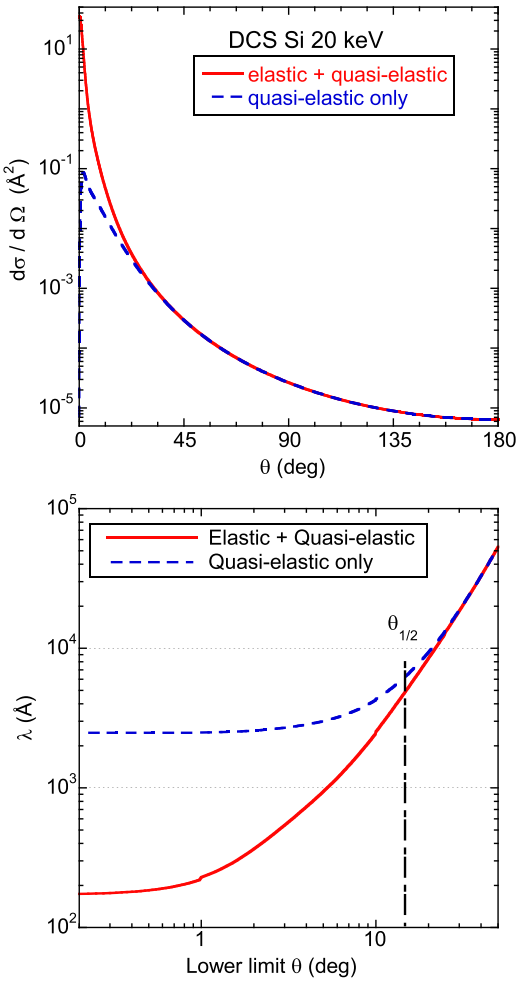

Figure 3. (Top) The differential cross section for 20 keV electrons as scattered from Si. The solid line is the total cross section, as calculated for a single atom using the partial wave formalism. The dashed line is the incoherent cross section only, based on the Debye–Waller factor of silicon. (Bottom) the quasi-elastic MFP as a function of the lower limit of integration in equation (6). An estimate of the incoherent MFP is obtained by either integrating the total DCS from the cut-off angle $\theta_{1/2}$ which gives ≈4600 Å, or by integrating the quasi-elastic cross section from 0 to π (2400 Å).

The mean-free-path between quasi-elastic, incoherent collisions is given by:

$$\lambda^{\text{quasi}} = \frac{1}{N\sigma_{\text{tot}}^{\text{quasi}}}. \tag{8}$$

In figure 3 we plot the differential cross section for 20 keV electrons scattered from Si, as calculated for an atom with the ELSEPA program [11] (total elastic) and after subtracting the coherent fraction (elastic incoherent). The lower panel shows the calculated quasi-elastic MFP, as a function of the lower limit of integration (equation (6)). Using a lower limit of 14.7°, as suggested by the Debye–Waller factor and integrating the total elastic DCS the quasi-elastic MFP becomes 5000 Å. Alternatively, if we use equation (7) to integrate only the incoherent part, but down to $\theta = 0$, we obtain an estimate for the quasi-elastic MFP of 2500 Å (see also table 1). We consider this argument semi-quantitative, and the fact that both approaches give an answer that is different by a factor of 2 reflects that. Both results, however, strongly suggest that the separation λ^{quasi} between incoherent quasi-elastic collisions in a crystal is an order of magnitude larger than implied by the total elastic cross section. Because the incoherent quasi-elastic events are localized at the atomic sites in the crystal, we take λ^{quasi} as the relevant mean free path for those collisions which create the Kikuchi diffraction sources.

2.2. Electronic excitations

For the description of the inelastic scattering (i.e. electronic excitations, either plasmons or electron–hole pairs with energy ω) we use the dielectric formalism [17, 19, 20]. This implicitly means that we assume that inelastic scattering does not depend on the direction of propagation of the electrons in the crystal. Near channeling conditions, this assumption is not fulfilled [21, 22], but it should suffice for getting at least a rough approximation. We start with the energy loss function (ELF) at $q = 0$ and use for the low-energy loss the results

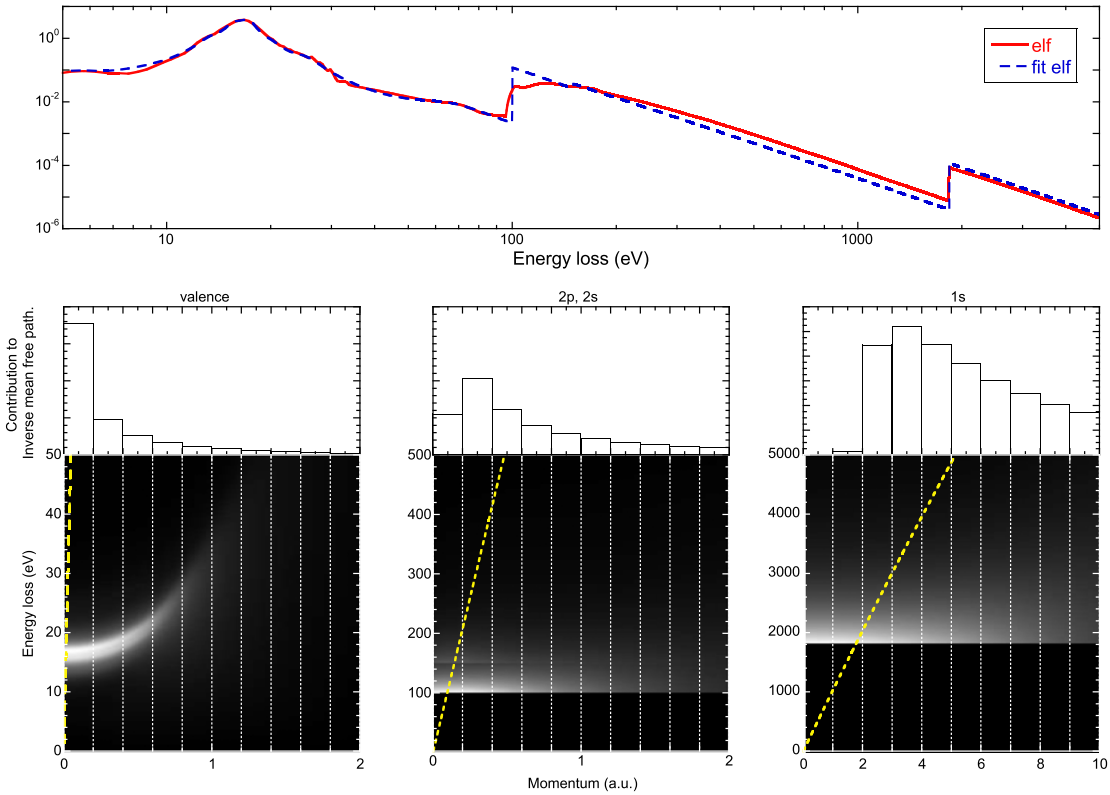

Figure 4. The ELF from Si, as fitted with Mermin loss functions for the valence and GOS (generalised oscillator strength), based on hydrogenic functions for the core electron (see e.g. [17]). The lower panel shows Im $[-1/\epsilon\,(\omega,\,q)]$, split for the valence band, semi-core and 1s contribution. The dashed line is the lower limit of the q integration in equation (10), again for 20 keV electrons. The central panel shows the distribution of inelastic scattering events over q for the case of 20 keV electrons as is obtained by evaluating the integral (equation (9)) over a limited range of q, as indicated by the dashed vertical lines in the lower panel.

Table 1. The elastic MFP for Si based on cross sections as indicated, as well as the inelastic MFP for the valence, semi-core and core electrons. The total inelastic MFP $\lambda^{\rm in}_{\rm tot}$ is calculated using $1/\lambda^{\rm in}_{\rm tot} = 1/\lambda^{\rm in}_{\rm v.b.} + 1/\lambda^{\rm in}_{\rm 2s,2p} + 1/\lambda^{\rm in}_{\rm 1s}$. The lowest row shows the total inelastic MFP according to the relativistic TPP (Tanuma, Powell Penn) theory [18].

Energy	10 keV (Å)	20 keV (Å)	30 keV (Å)	40 keV Å
$\lambda^{\rm el}_{\rm tot}$ (Equation (1))	92	172	251	315
$\lambda^{\rm quasi}_{\rm tot}$, (Equation (6))	2461	4907	7166	9062
$\lambda^{\rm quasi}_{\rm tot}$, (equation (7))	1313	2481	3568	4555
$\lambda^{\rm in}_{\rm v.b.}$	178	320	447	564
$\lambda^{\rm in}_{\rm 2s,2p.}$	1394	2351	3193	3955
$\lambda^{\rm in}_{\rm 1s}$	1.95×10^5	2.87×10^5	3.73×10^5	4.46×10^5
$\lambda^{\rm in}_{\rm tot}$	158	281	391	493
$\lambda^{\rm in}_{\rm tot}$ TPP	156	277	386	485

from Jin [23] as an estimate of the ELF and at larger energy losses the tabulation from Henke [24]. These were fitted with Mermin loss functions for the valence band loss features and generalized oscillator strength (GOS) for the 2p, 2s and 1s core electrons as described in [25]. The result is shown in the top panel of figure 4. In this way we get a description of Im$[-1/\epsilon(q,\omega)]$ everywhere in (q,ω) space, see the lower panels of figure 4. From Im $[-1/\epsilon\,(q,\,\omega)]$ one can calculate the probability of inelastic scattering per unit path length using [26]:

$$1\,/\,\lambda^{\rm in} = \int_0^{E_0} \frac{{\rm d}\omega}{\pi E_0} \int_{q_-}^{q_+} \frac{{\rm d}q}{q}\,{\rm Im}\left[\frac{-1}{\epsilon\,(q,\,\omega)}\right], \tag{9}$$

with

$$q_\pm = \sqrt{2mE_0} \pm \sqrt{2m(E_0 - \omega)}. \tag{10}$$

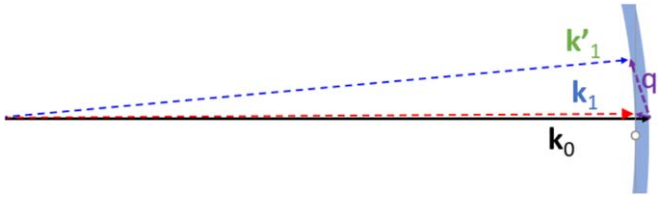

Figure 5. Kinematics of electron energy loss ω. After the energy loss the magnitude of electron momentum k_1 is slightly less than k_0, which means that the magnitude of the momentum transfer $\boldsymbol{q}$ is always finite.The probability of energy loss of ω per unit path length is obtained by integrating Im $[-1/\epsilon\,(q,\,\omega)]$ over the range of possible q values(see equation (9)). For the case of Si plasmon creation by 20 keV electrons the length difference between k_0 and k_1 is very small and exaggerated in the drawing, for clarity. Most of the contributions to the inverse mean free path (equation (9)) is for q values close to q_{min}.

(with m the electron mass) corresponding to the minimum and maximum momentum transfer at $\theta = 0$ and $\theta = \pi$ respectively.

We start by considering inelastic scattering from valence electrons. For small q values, the energy loss is due to plasmons (long range density fluctuations in the electron gas), and for large q, one scatters from individual valence electrons and creates electron–hole pairs.

In figure 4, the integral of equation (9) is split up over several momentum intervals in order to see how the contribution for the various q ranges varies. For the scattering by valence band electrons, the electron losses occur mainly at very low q values via plasmon creation, with a tail due to electron–hole excitations extending to larger q values. The corresponding inelastic MFP is given in table 1.

The precision with which one can determine the location of the scattering event is of the order of $1/q$ as follows from the Heisenberg uncertainty relation. For small q values, the collision is effectively delocalized over the unit cell and as a consequence the projectile does not get localized with crystallographic resolution due to plasmon excitation. For large q values, the collision is localized at the position of the valence electron. The valence electron distribution, however, is fairly uniform over the unit cell, for Si with some enhancement between nearest neighbours due to the chemical bond. The scattered electrons appear thus to originate from either the whole of the unit cell (plasmons) or from a broad area mainly away from the nuclei (electron–hole excitations) and the corresponding diffraction contrast will be weak and different from the electrons scattered from the nuclei (see figure 2).

If one assumes that coherence would be totally lost by valence band inelastic excitations, then there would be no contrast expected after such an event. This is not the case, as will be seen below for reflection measurements, but is also observed in transmission electron microscopy (TEM) [27] and discussed by Howie [28, 29].

Concerning the effect of plasmon scattering on Kikuchi electrons, the necessary preservation of the initial localization information in the unit cell will be limited by the degree of preservation of the relative phase of the electron waves contributing to the Kikuchi pattern. Thus, plasmon scattering on the outgoing path after the initial localized Kikuchi source event can possibly preserve this information if all waves are scattered by the same plasmon excitation [29]. However, because momentum transfer by plasmon scattering can also slightly change the direction of the electron waves (figure 5), the localization information for a specific observation direction on the detection screen will tend to be averaged out by multiple plasmon scattering events [30]. From these arguments, we can assume that Kikuchi pattern contrast is not lost immediately with the first plasmon loss, but will gradually reduce with an increasing number of plasmon scatterings on the outgoing path. The situation is much clearer with inelastic scattering on the ingoing path, which influences the Kikuchi pattern only via the change of wavelength, and the Kikuchi source localization at an atomic site can still occur after an arbitrary number of plasmon losses.

For the Si semi-core electrons (2s, 2p) with binding energies of 100 eV and 150 eV, respectively, the contribution to the ELF extends over a larger q range, and hence will generally be more localised. As these electrons are at the atomic positions, the corresponding diffraction pattern will be similar to that after large-angle elastic scattering but could be somewhat more diffuse as the corresponding momentum transfer is smaller. The MFP for 2s, 2p excitation is about 7–8 times longer than for valence band (plasmon) excitations. The energy loss in a 2s, 2p electron excitation is about 8 times larger. Thus both processes contribute a similar amount to the electron stopping (mean energy loss per unit distance travelled).

Finally, the 1s core level contribution to energy loss events is at much larger q values, but these are infrequent events and the mean distance between 1s electronic excitations is huge. Its contribution to the diffraction pattern will be similar to that after large-angle elastic scattering but the corresponding intensity will be negligible small.

2.3. Kikuchi contrast and the dynamical theory of diffraction

The observed Kikuchi contrast in EBSD can be simulated using the the Bloch wave approach of the dynamical theory of electron diffraction. As described in [31, 32], the model assumes that EBSD Kikuchi patterns can be described by an effective energy near the primary beam energy, and the effects of inelastic and incoherent scattering on the Kikuchi patterns are considered only in so far as they can be handled via an imaginary potential that describes reduction of the coherent pattern intensity by plasmons and phonons.

For a Kikuchi electron source at position $\mathbf{r}_S$ in the crystal, the EBSD Bloch wave approach discussed in [31, 32] calculates the intensity of the approximate plane wave with wave vector $\mathbf{K}_0$ which is observed in the direction $\mathbf{K}_0/|\mathbf{K}_0|$ on the detector screen. Using the reciprocity principle [33, 34], the wave function at the detector can be calculated by starting a reversed plane wave and calculating the scattered wave function $\Psi(\mathbf{r})$ at the Kikuchi source point $\mathbf{r}_S$.

The wave function $\Psi(\mathbf{r})$ of an incident plane wave $\mathbf{K}_0$ can be written as the sum of contributions of scattered plane waves $\exp[2\pi\mathrm{i}(\mathbf{K}+\mathbf{g})\cdot\mathbf{r}]$ moving into directions $\mathbf{K}+\mathbf{g}$ and having a depth t dependent amplitude $\phi_{\mathbf{g}}(t)$:

$$\Psi(\mathbf{r}) = \sum_{\mathbf{g}} \phi_{\mathbf{g}}(t)\ \exp[2\pi\mathrm{i}(\mathbf{K}+\mathbf{g})\cdot\mathbf{r}] \tag{11}$$

with $\mathbf{K}$ describing the incident beam $\mathbf{K}_0$ corrected for refraction when entering the crystal [35].

The variation of the Kikuchi intensity from a source at $\mathbf{r}_S$ is thus essentially determined by the probability density $P(\mathbf{r})$ as a function of the detected direction:

$$P(\mathbf{r}_S) = \Psi(\mathbf{r}_S)\Psi^*(\mathbf{r}_S) \equiv \sum_{\mathbf{g},\mathbf{h}} a_{\mathbf{g}}(\mathbf{r}_S)a_{\mathbf{h}}^*(\mathbf{r}_S) \tag{12}$$

and the comparison with equation (11) shows that the variation in $P(\mathbf{r}_S)$ can be seen to result from interference terms $a_{\mathbf{g}}(\mathbf{r}_S)a_{\mathbf{h}}^*(\mathbf{r}_S)$ related to the scattering of the incident beam by the reciprocal lattice vectors $\mathbf{g}$, $\mathbf{h}$.

Electrons entering the crystal in a direction far from any diffraction plane will maintain their original plane-wave character, i.e. the effect of the crystal on $P(\mathbf{r}_S)$ for $\mathbf{g} \neq (000)$ is low. Near the Bragg condition, the corresponding eigenfunctions in the crystal are standing waves with either the maximum density at the atom position (type 1 waves) or the minimum at the atom position (type 2 waves) [35]. For typical conditions in an EBSD experiment, the type 1 waves will be dominant for angles slightly less than the Bragg angle, while type 2 waves will be dominant for slightly larger angles. This leads to Kikuchi bands with increased intensity in a width of twice the Bragg angle centered on the relevant lattice plane.

One of the parameters in such a calculation is the range of depths t one has to consider. This is usually chosen empirically so the level of detail in the diffraction pattern agrees with the experiment. If one only considers small t values, the pattern is blurred due to reduced multiple scattering, and for very large t values, there will be contrast inversion of the Kikuchi bands due to anomalous absorption [36]. Such contrast inversion is also seen in transmission experiments with increasing crystal thickness [37] or in photoelectron diffraction as a function of energy loss [38, 39]. Empirically, by choosing a t range of the order of the inelastic MFP [36], one obtains reasonable agreement with either the Kikuchi pattern as seen using an electrostatic analyzer or observed on a phosphor screen.

3. Experimental details

The experiments described here were carried out at an initial electron energy E_0 of 30 keV. A 500 eV beam was produced by an electron gun (BaO cathode 0.4 eV energy spread). The sample is held at 29.5 keV in a high-voltage sphere and thus 30 keV electrons impinge on the sample. Ripple and drift of the main high-voltage supply do not affect the measurement as the same potential that accelerates the electrons while entering the sphere, decelerates them while going into the analyser. The detector is placed at 45° with respect to the incoming beam direction and measures both the electron energy and the ϕ-angle. Electron detection is done with a pair of channel-plates in combination with a phosphor screen. Individual electrons are detected and analysed for their energy and angle. The noise in the 'image' obtained in this way is statistical, i.e. the square root of the number of electrons detected at a certain energy-angle combination.

The sample is rotated over 0.2° steps under computer control, and a measurement of the ϕ intensity distribution is done at each angle. The scan starts with the incoming beam glancing in ($\theta_{\mathrm{in}} \approx 85°$ with the surface normal and $\theta_{\mathrm{out}} \approx 50°$) and ends when the sample has rotated over 35° and $\theta_{\mathrm{in}} \approx 50°$, $\theta_{\mathrm{out}} \approx 85°$ and then the detected electrons are glancing out. The measurement at each angle is done for the same amount of accumulated charge. The analyser can be tuned to the energy of the incoming beam (elastic peak), or to a lower energy. Thus one can collect, in different scans, the Kikuchi profiles of electrons with different energy losses. The energy resolution was 0.5 eV. For more details see [40, 41].

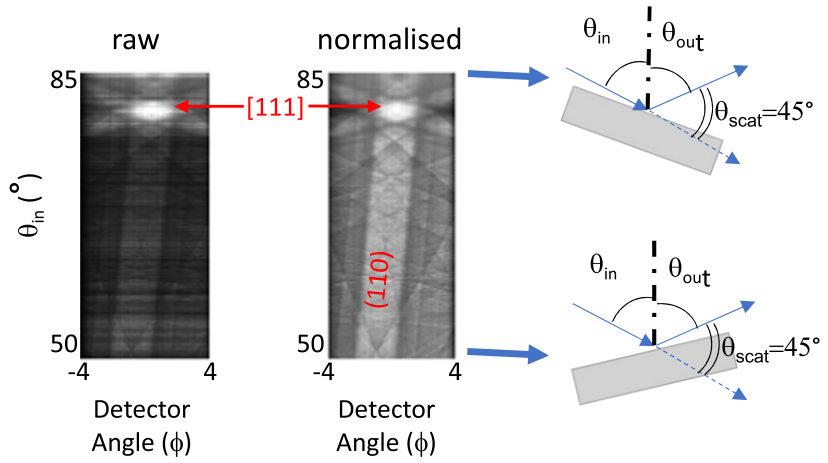

Figure 6. The raw intensity, as measured for a range of incident beam angles (θ) over a range of detector angles (ϕ) as measured (left) and after normalisation to the same number of counts for each θ angle (center). This largely removes the effect of channeling of the incoming beam. The right panel illustrates how the scattering geometry changes if the sample is rotated.

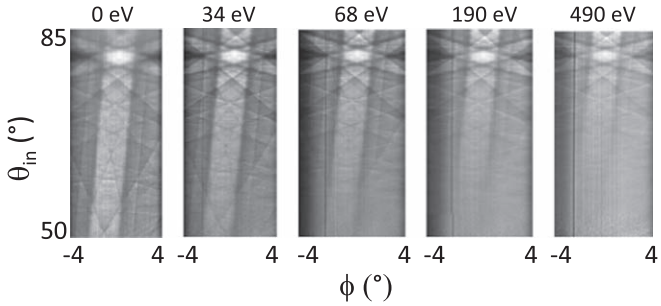

Figure 7. Kikuchi distributions measured for several energy loss regions, centered at values indicated. The vertical dark lines seen near $-3°$ for the measurements at larger energy losses are due to detector artifacts.

4. Experimental results

The result of a scan for the elastic peak is shown in figure 6. As the sample rotates, also the incoming beam direction changes, and hence the backscattered intensity varies, depending on the channeling conditions of the incoming beam [41]. The total number of counts acquired for a certain orientation reflects this. It was found that the obtained Kikuchi pattern is more clearly defined if the angular distribution acquired for each crystal orientation is normalized to the same number of counts, i.e the channeling effect of the incoming beam is removed. This normalization procedure is illustrated in figure 6 as well. Especially after this normalization one can see a well-defined Kikuchi band with a nearly vertical orientation. This is the Kikuchi band from the (11 0) plane. For $\theta_{\rm in} = 80.5°$ the [1 1 1] zone axis points towards the detector. For the zone axis the count rate is much larger. The normalization procedure used causes an artificial reduction in intensity away from the zone axis, i.e. for very small and large ϕ values near $\theta_{\rm in} = 80.5°$ (darker triangles at left and right from zone axis).

The analyser potential was adjusted so electrons with different energy losses were transmitted through the analyser and the corresponding intensity distributions were recorded and are, after normalisation, displayed in figure 7. There is a strong difference in the energy loss dependence for large and small $\theta_{\rm in}$ values. For the largest $\theta_{\rm in}$ values the contrast first increases with energy loss but for smaller $\theta_{\rm in}$ values the contrast is maximum at zero energy loss. This becomes even more evident for the profiles plotted in figure 8. In the glancing out geometry very little contrast survives for energy losses larger than 100 eV.

At even larger energy losses the contrast is weaker and becomes less than the statistical noise. Applying a FFT band pass filter, we still can discern some contrast, as is clear in figure 9 where both the elastic and 2 keV loss distributions are shown after the same FFT band-pass filter was applied. At the largest $\theta_{\rm in}$ angles, the contrast in the elastic peak and 2 keV loss distribution is very similar. At intermediate angles the band contrast disappears, but dark and light lines appear at the edge of the bands [33]. For the smallest $\theta_{\rm in}$ angles (i.e. glancing out condition) the main band (1 1 0) is darker, i.e. displays a weak, inverted contrast.

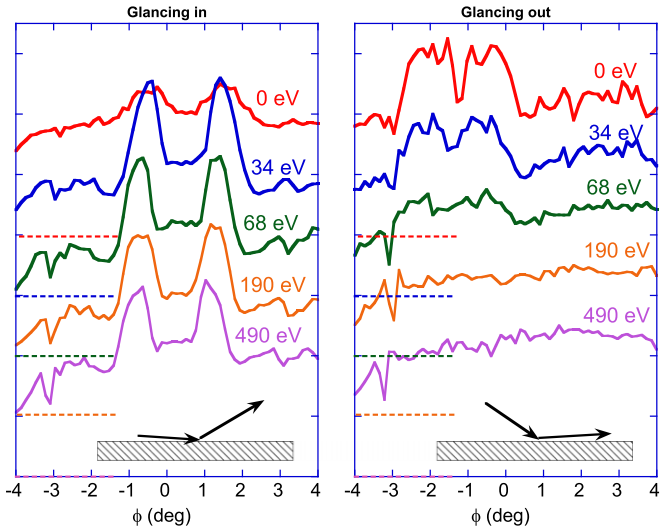

Figure 8. Profiles as measured as a function of energy loss for a glancing in ($\theta_{in} = 84°$) and glancing out geometry ($\theta_{in} = 49°$). (Near the extremes of figure 7).

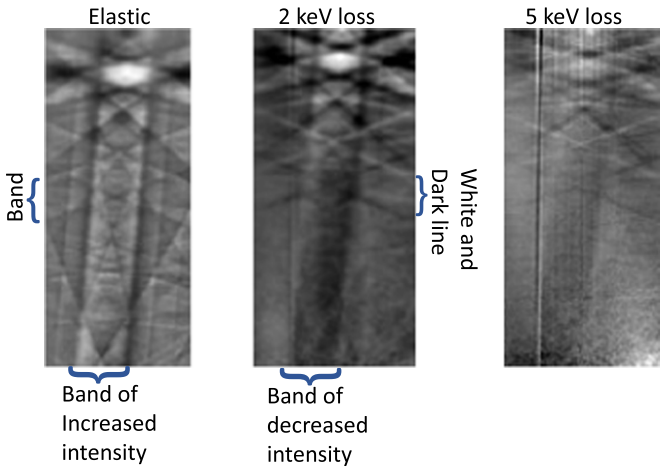

Figure 9. A comparison of the distribution as measured at 0, 2 and 5 keV energy loss. In order to reduce the noise both images were filtered using a FFT band pass filter.

At 5 keV energy loss (and also at 10 keV, not shown here), the contrast is even weaker and, after adjusting the contrast of the image to compensate for that, the detector artifacts, observed as vertical lines become more pronounced. Note that the intensity near the [1 1 1] direction, which was the most intense at lower energies, is now less pronounced. Absorption effects are becoming evident for this direction as well.

5. Discussion

The spectrometer geometry dictates that all detected electrons have at least scattered over 45°. If we make the simplifying assumption that the trajectories are approximately v-type (only 1 large-angle deflection of ≈45°, with possible other deflections but over considerably smaller angles) then one can distinguish an incoming and an outgoing trajectory (see figure 10). V-type trajectories have been shown to be a good approximation for backscattering of high energy electrons with relatively low energy losses, but longer trajectories, in particular for lower energy (sub-keV) electrons are more complex [42, 43]. For an electron that reached depth x the incoming and outgoing path length are then approximately $x/\cos(\theta_{in})$ and $x/\cos(\theta_{out})$. The outgoing path length L_{out} is then related to the total path length L by:

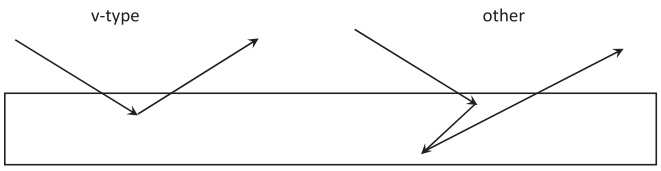

Figure 10. A v-type trajectory (left) and a more complex trajectory (right).

$$L_{\text{out}} = \frac{1/\cos\theta_{\text{out}}}{1/\cos\theta_{\text{out}} + 1/\cos\theta_{\text{in}}} L = \eta_o L \tag{13}$$

with η_o the fraction of the total path length that is along the outgoing trajectory. For $\theta_{\text{in}} = 85°$, the outgoing trajectory is ten times shorter than the incoming. This applies to the top of figure 7 and the left panel of figure 8. For $\theta_{\text{in}} = 50°$ (and hence $\theta_{\text{out}} = 85°$) it is the other way around, the outgoing trajectory is 10 times longer (bottom of figure 7 and the right panel of figure 8).

For the elastic peak measurement the sum of the incoming and outgoing pathlength will be, on average, about the inelastic MFP ($\lambda^{\text{in}} \approx 410$ Å at 30 keV). For a measurement at an energy loss corresponding to n plasmon losses (the plasmon energy of Si is 17 eV) the mean path length is then $\approx(n + 1)\,\lambda^{\text{in}}$. Thus for each θ_{in} value and energy loss one can estimate the average outgoing path length. The fact that the Kikuchi pattern only gradually develops with energy loss for $\theta_{\text{in}} \approx 85°$ and persists up to very large losses is thus a consequence from the very short outgoing path length. For $\theta_{\text{out}} \approx 85°$ almost all energy losses occur along the, much longer, outgoing trajectory, and indeed in this case the contrast is maximum for the elastic peak and decreases with energy loss.

Looking at the angular distributions for the glancing out measurement it becomes obvious that not all contrast is lost after a single plasmon excitation. For 34 eV energy loss (corresponding to 2 plasmons) and even 64 eV energy loss (4 plasmons) there is still diffraction contrast in the glancing out geometry, and the probability that all plasmons are created along the (in this geometry very short) incoming trajectory is negligible small.

One way one can understand the influence of the plasmon excitation on the Kikuchi contrast is angular broadening. The plasmon creation changes slightly the direction of propagation of the electron. As a consequence the observed Kikuchi pattern after creation of n plasmons is the n-fold convolution of the Kikuchi pattern with the momentum distribution of the plasmon. Here, one makes the simplifying assumption that the change in direction somewhere along a trajectory can be modelled by angular broadening of the calculated distribution after the electron has left the sample. This is shown in figure 11 for the glancing out results of figure 8 where almost all plasmons are created along the outgoing path. This simple approach gives roughly the right rate of decrease in contrast with increasing energy loss.

For glancing in measurements the outgoing trajectory is first too short for significant diffraction contrast to build up. The contrast is maximum for 34–68 eV energy loss and decreases subsequently very slowly. At 34 eV energy loss the mean path length will be 3λ (1200 Å) and hence the outgoing trajectory will have a length for small θ_{in} values or the order of 120 Å, which appears enough for the build up of the contrast to be realized.

However, it is also clear that the nature of the observed pattern changes with energy loss, not just the level of contrast. The contrast disappears slowly with energy loss and then reverses with energy loss for glancing out directions. The excess and deficit Kikuchi lines become much more pronounced.

5.1. Kikuchi contrast model

Our experimental observations can be rationalized using the analysis of the elastic and inelastic cross sections discussed in in section 2. As we will see, the fact that the quasi-elastic mean free path is about an order of magnitude larger than the inelastic mean free path limits the effective energy range contributing to the Kikuchi pattern contrast. Basically, with increasing total energy losses, longer total path lengths will be required to excite the corresponding number of plasmons, and a larger absolute number of these plasmons will tend to occur on the outgoing path, generally decreasing the diffraction contrast with increasing energy loss.

A key approximation of the model is that the trajectories of backscattered electrons with low energy losses are assumed to be effectively of the v-type, involving a single large-angle backscattering event that changes the electron direction to end up in the detector, as discussed more extensively in the previous section. For a fixed scattering angle of detection, the relative probabilities $p_V(L)$ of the different v-type trajectories with total path length L can be determined from the properties of Poisson processes. The probability distribution of the total path length $L = L_{\text{in}} + L_{\text{out}}$ is the product of the probability distribution of the ingoing path lengths L_{in} until a single event is observed, and the probability of not having any another event on the outgoing path length L_{out}. Both of these probabilities are proportional to exponential functions and we can thus define:

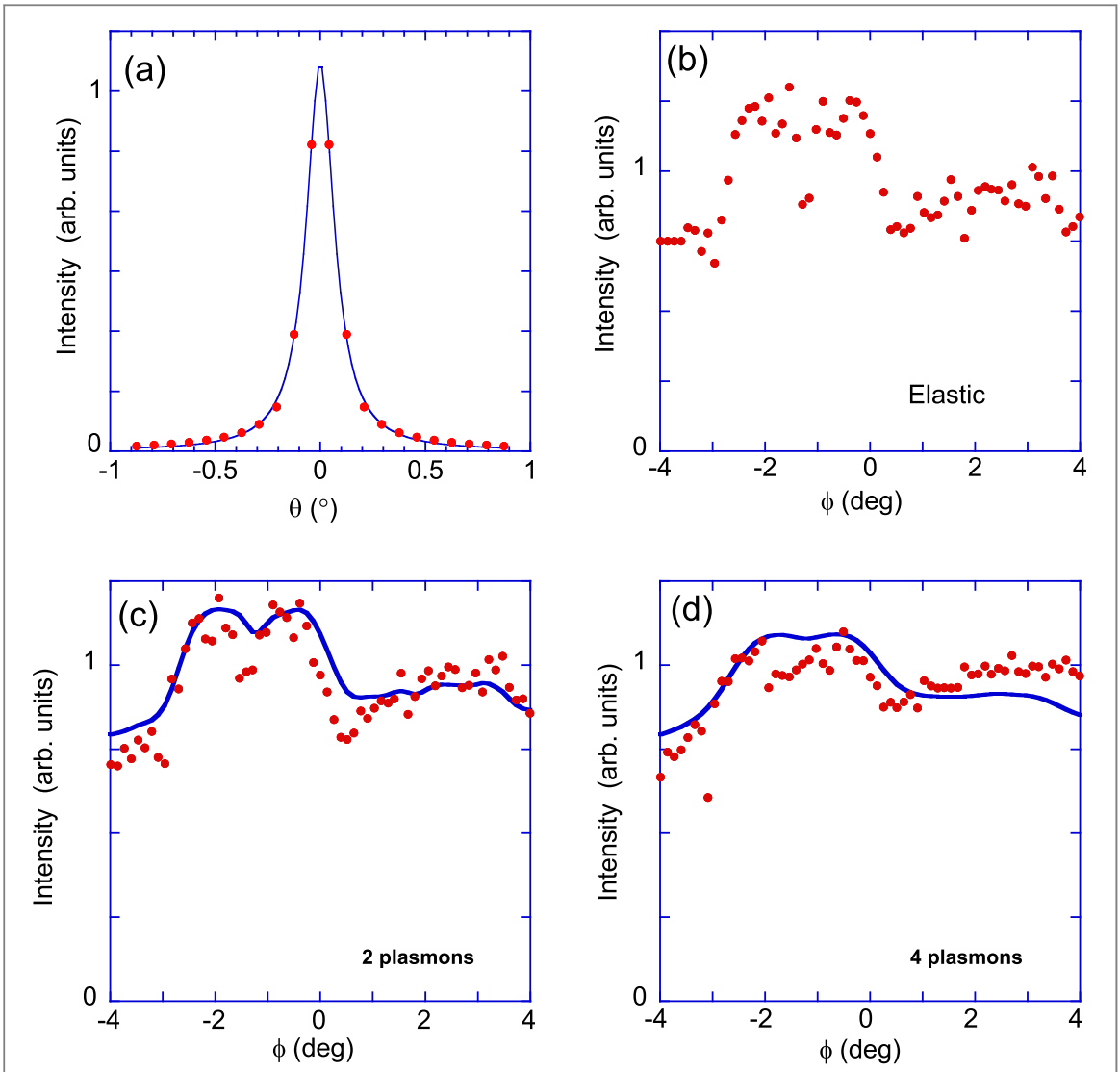

Figure 11. (a) Probability distribution of momentum transfer during plasmon excitation (dots), fitted with a Lorentzian (line). (b) Kikuchi profile for an energy loss corresponding to the creation of 2(c) and 4(d) plasmons (dots) together with Kikuchi profile for the elastic peak convoluted twice (c) and four times (d) with the broadening function for plasmon creation (lines).

$$p_V(L) = \mathrm{e}^{-L_{\mathrm{in}}/\lambda^{\mathrm{quasi}}}\mathrm{e}^{-L_{\mathrm{out}}/\lambda^{\mathrm{quasi}}} = \mathrm{e}^{-L/\lambda^{\mathrm{quasi}}}. \tag{14}$$

The relative probability of total v-type path lengths with a mean free path $\lambda^{\mathrm{quasi}} = 350$ nm for quasi-elastic, incoherent scattering events is shown in figure 12(a). For our experimental scattering geometry, the v-type approximation is expected to work well for path lengths up to the order of λ^{quasi} but significant deviations could occur for longer ones.

The second assumption of our model is that on a given trajectory of total length L, the excitation of n inelastic events is given by the Poisson distribution for the inelastic mean free path λ^{in}, independently of the elastic scattering events:

$$p_n(L) = \frac{(L/\lambda^{\mathrm{in}})^n}{n!}\,\mathrm{e}^{-L/\lambda^{\mathrm{in}}}. \tag{15}$$

The relative probability of path lengths with a number of inelastic events with $\lambda^{\mathrm{in}} = 40$ nm is shown in figure 12(b).

The total probability $p_{nV}(L)$ for a v-type path of total length L with n inelastic losses is thus:

$$p_{nV}(L,\ \lambda^{\mathrm{in}},\ \lambda^{\mathrm{quasi}}) = p_n(L,\ \lambda^{\mathrm{in}})\ p_V(L,\ \lambda^{\mathrm{quasi}}) \tag{16}$$

with $p_{0V}(0,\ \lambda^{\mathrm{in}},\ \lambda^{\mathrm{quasi}}) = 1$, see figure 12.

We assume that the Kikuchi diffraction is operating on the geometrical outgoing fraction η_o of the v-type path, which is related to the total path length by equation (13). In our experimental geometry, each possible trajectory is uniquely defined by the angles θ_{in} and θ_{out} and one of the lengths L, L_{in}, or L_{out}. This is why the distribution of the outgoing path length L_{out} is fixed to the respective distribution of the corresponding total path

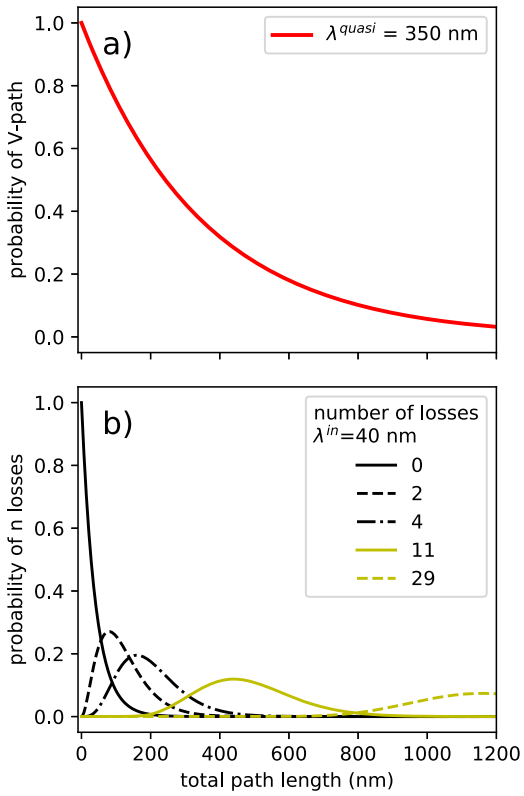

Figure 12. (a) Probability distribution $p_V(L)$ of total v-type trajectory lengths L which contain exactly one quasielastic incoherent scattering event with mean rate $\lambda^{\text{quasi}} = 350$ nm. (b) probability distribution $p_n(L)$ of total trajectory lengths considering the creation of a given number of plasmons with mean rate $\lambda^{\text{in}} = 40$ nm.

length $L = L_{\text{out}}/\eta_o$. Combined with the relative probability $p_{nV}(L, \lambda^{\text{in}}, \lambda^{\text{quasi}})$ for the total path length with a given number of energy losses on the v-type trajectory, we can thus determine the distribution $\sigma_o(L_{\text{out}})$ of outgoing lengths L_{out} which are relevant for the Kikuchi diffraction mechanism:

$$\sigma_o(L_{\text{out}}) = p_{nV}(L_{\text{out}}/\eta_o(\theta_{\text{in}}, \theta_{\text{out}}), \lambda^{\text{in}}, \lambda^{\text{quasi}}). \tag{17}$$

The distribution $\sigma_o(L_{\text{out}})$ enters into the calculation of the dynamical Kikuchi diffraction effects as a weight factor which treats the varying contribution of Kikuchi sources according to the possible outgoing path lengths and the total number of discrete energy losses. In figure 13, we show the resulting distributions for different outgoing angles and assuming different numbers of discrete energy losses according to the parameters shown in figure 12. This figure illustrates that an increasing total energy loss implies a larger outgoing path length for a given geometry, and we see that the relative contribution of trajectories is strongly decreasing as a function of the number of energy losses.

Considering Kikuchi diffraction effects, we need to consider that an increasing number of inelastic scatterings n_o on the outgoing path length L_{out} will lead to a reduction of diffraction contrast. In the Bloch wave model, this can be handled by a reduction the off-diagonal interference terms in equation (12) by a coherence factor $\gamma_C(L_{\text{out}})$:

$$P(\mathbf{r}_S) = \sum_{\mathbf{g},\mathbf{h}} \gamma_C(L_{\text{out}})\, a_{\mathbf{g}}(\mathbf{r}_S) a^*_{\mathbf{h}}(\mathbf{r}_S). \tag{18}$$

We assume that $\gamma_C(L_{\text{out}})$ reduces the interference contrast of different plane waves by an exponential factor that only depends on the length L_{out} of the outgoing path:

$$\gamma_C(L_{\text{out}}) = \begin{cases} \exp(-L_{\text{out}}/\lambda_C) & \text{if } \mathbf{g} \neq \mathbf{h} \\ 1 & \text{if } \mathbf{g} = \mathbf{h} \end{cases}. \tag{19}$$

The value of λ_C describes how effective the inelastic scattering processes are in reducing the interference contrast after the initial quasi-elastic scattering event. Using the parameter λ_C, we can thus model a reduction of the relative spatial variation of the exit probability in the unit cell.

As an additional effect which concerns long path lengths, the effect of contrast inversion of Kikuchi bands by anomalous absorption is also reproduced by the Bloch wave simulations [10, 36]. However, the possible additional multiple diffuse scattering of those electrons which have been 'anomalously absorbed' is not treated

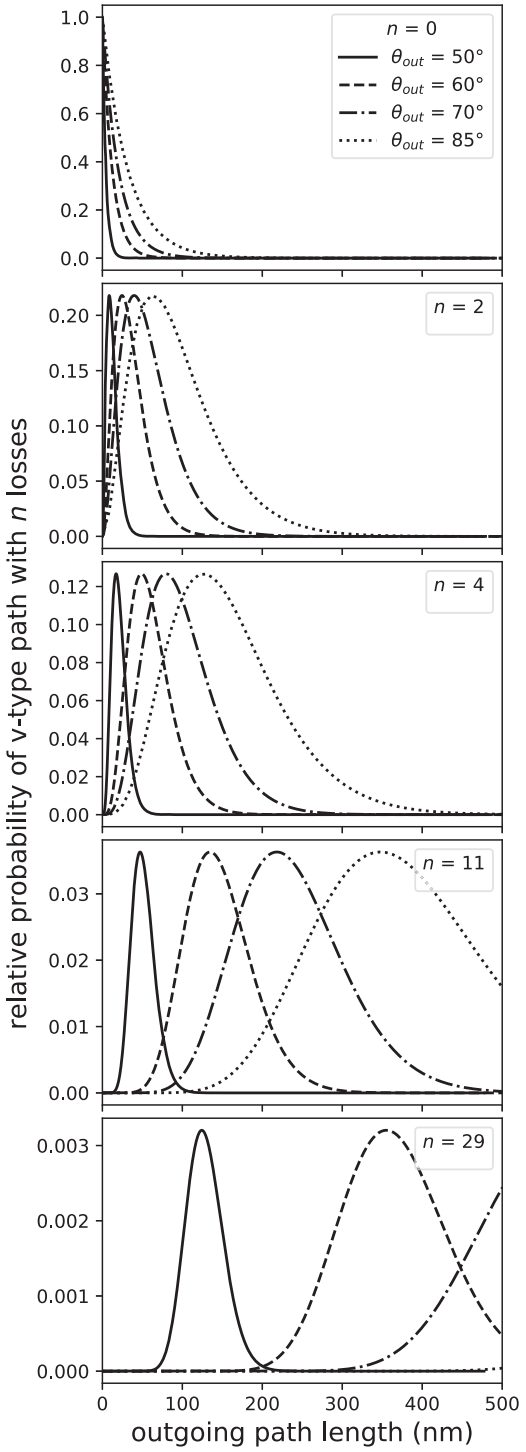

Figure 13. Relative contribution of outgoing path lengths in the experimental geometry with outgoing angles θ_{out}. These curves are obtained by the product of the probability distributions in figures 12(a) and (b) and by assigning the outgoing path length to the respective values of the total path in figure 12. In the Kikuchi diffraction model, these curves weight the distances over which diffraction occurs from the incoherent point sources.

in the idealized simulations using an imaginary potential. As a result, the predicted magnitude of the contrast inversion can be larger than observed in reality, because the contribution of diffusely scattered electrons from other directions reduces the observed contrast. This is why we treat the effect of reduced anomalous absorption contrast by a phenomenological factor $\gamma_A(L_{out})$ which reduces the size of the absorptive electron scattering factors $f_0'(s)$ [44, 45] according to the outgoing path length:

$$f'(s, L_{out}) = \gamma_A(L_{out}) f_0'(s), \tag{20}$$

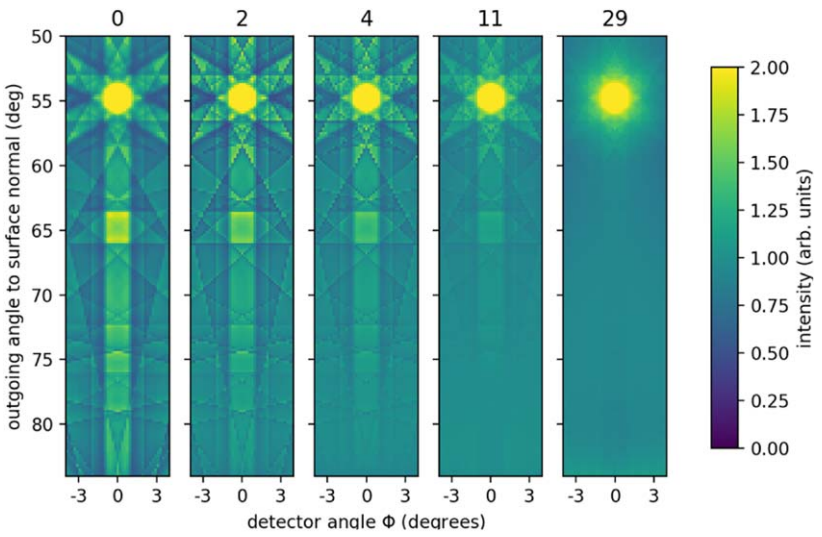

Figure 14. Calculated Kikuchi patterns approximating the case of figure 7. The single quasielastic backscattering events on the v-trajectories are assumed to occur with a mean free path $\lambda^{\mathrm{quasi}} = 350$ nm and plasmons are created with $\lambda^{\mathrm{in}} = 40$ nm (number of losses indicated on top). The decoherence length for the Bloch wave intensity in the unit cell was $\lambda_C = 3.0\lambda^{\mathrm{in}}$, and the reduction length for the absorptive scattering factors $\lambda_A = 4.0\lambda^{\mathrm{in}}$ as explained in detail in the text.

$$\gamma_A(L_{\mathrm{out}}) = \exp(-L_{\mathrm{out}}/\lambda_A). \tag{21}$$

The factor $\gamma_A(L_{\mathrm{out}})$ thus works as an additional overall reduction of the Debye–Waller factor in the calculation of the Fourier coefficients U'_g of the imaginary part of the crystal potential [45], scaling the overall effect of anomalous absorption and anomalous transmission.

Using the v-type trajectory model with the parameters λ^{quasi}, λ^{in} derived from theory, and with the two phenomenological parameters λ_C, λ_A, we can obtain a good qualitative description of our complete experimental data with only 4 parameters. In figure 14, we show simulations assuming the following values $\lambda^{\mathrm{quasi}} = 350$ nm, $\lambda^{\mathrm{in}} = 40$ nm, $\lambda_C = 3\lambda^{\mathrm{in}}$, and $\lambda_A = 4\lambda^{\mathrm{in}}$. Because of the relatively broad path length distributions as shown in figure 13, the qualitative trends shown in figure 14 are preserved even for relatively large variations (±20%) in the assumed parameters. This illustrates the difficulty of extracting precise parameters concerning the distributions of path lengths and energies from experimental EBSD data without additional limiting assumptions [4, 36].

As a general trend, the model reproduces the progressing reduction of contrast towards shallow outgoing angles with increasing energy loss, including the experimentally observed trend to contrast reversal (e.g. lower parts for 11 and 29 losses; see also figure 9).

In addition to the loss of diffraction contrast by inelastic scattering, the model also reproduces the loss of Kikuchi pattern sharpness due to a reduced interaction volume for the elastically scattered electrons in a glancing-in geometry, i.e. the zone axis feature near $\theta_{\mathrm{out}} = 55°$ in figure 14 is sharper for 2 plasmon losses than for no losses. As has been discussed before [46], after a few plasmon scatterings on the glancing ingoing path, the Kikuchi patterns are created sufficiently deep inside the crystal for a sharp pattern to develop.

The model parameters are in a range which is consistent with the discussion of the elastic and inelastic cross sections in section 2 and the available knowledge concerning the reduction of interference contrast by inelastic scattering events. The magnitude of $\lambda_C \approx 3\lambda^{\mathrm{in}}$ is consistent both with the partial preservation of contrast after only a few plasmon scatterings, as well as with the long-range limit of suppression of diffraction contrast by multiple plasmon scatterings. As has been discussed in section 2.2, the core losses will become important when large energy losses are observed, and thus we cannot expect our simple model to be valid beyond the energy range of 0.5–1 keV. Also, the the v-type approximation is not a good approximation for the longer trajectories associated with events at larger energy losses.

Comparing our model with the experimental trends, the same trends are observed in both. It appears thus that the electron distribution over energy and momentum in a sample is created by a rather complex interplay of multiple elastic and inelastic scattering processes, as described in the model. Our model does not aim to describe the detailed microscopic scattering dynamics of energy- and momentum exchanges and their influence on wave coherence. Instead, we provide an approximation for the final effects of the scattering processes on the electrons which are observed outside the sample.

6. Comparison to other experiments

The first measurement of 'energy-resolved Kikuchi bands' was done by Boersch, as early as 1953 [47]. Kikuchi bands where measured in a transmission geometry using a low-pass filter. If only electrons were transmitted with an energy loss less than 4eV he observed that the diffraction spots remained whereas the Kikuchi lines disappeared. From this he concluded that the formation of Kikuchi lines depended on electronic excitations, and could not be caused by just phonon excitations. From our measurements we understand that the intensity of the Kikuchi pattern should decrease (relative to the diffraction spots, as the contribution to the contrast with non-zero energy loss is suppressed) for such a low-pass filter but expect part to remain, as indeed we see very clear Kikuchi patterns for the elastic peak, in particular when the incoming beam is not glancing. Our observation is also in contrast to that of Deal *et al* [48] who also used a low-pass filter and report (using 15 keV electrons) reduced contrast when only electrons are transmitted with energy loss less than 500 eV. Their geometry is with the incoming beam rather glancing, but in our case full contrast is already seen at 38 eV energy loss, even under severe glancing in conditions.

It is of interest to compare the behaviour seen here with that measured in transmission Kikuchi measurements, e.g. the recent work of Brodu *et al* [37]. Within the v-type approximation we can compare the Kikuchi pattern as observed (at a certain energy loss and angle) for a certain outgoing path length in reflection with that obtained for this thickness in transmission. Indeed similar results are found. For short path length we see excess bands, for larger pathlength the excess and deficit lines becomes the most salient feature, and at the largest pathlength contrast reversal is seen. In our experiment for 2 keV energy loss the pathlength is about 1.2 μm (assuming the stopping of 0.17 eV/Å for 30 keV electrons [49] is not affected by the direction of propagation). In the experiment by Brodu *et al*, contrast inversion is seen for path lengths of 0.3 and 1 μm. As their experiment used 15 keV electrons, half the present energy, one would expect contrast reversal in our case for outgoing path length over 0.6–1.7 μm. Indeed contrast reversal is seen in figure 9 for incoming angles larger than 20°, where more than half of the total path length is along the outgoing trajectory.

Moore *et al* measured bent contour contrast as a function of energy loss [50]. He observes that the bent contrast (an interference effect) gradually becomes less sharp and weaker with energy loss but remains visible up to 1 keV energy loss, developing in a way not too different from figure 7 and the effect of the momentum transfer in the inelastic excitations is modelled as an effective increase in the angular spread of the incoming beam.

In the study by Ram and de Graef [51], it was suggested by Monte-Carlo simulations that electrons with a relative large range of energies (down to ≈30% of the incoming energy) contribute significantly to the Kikuchi contrast according to their intensity in the simulated BSE spectrum. From our experimental measurement, we conclude that at correspondingly large losses, the contrast is very weak relative to the background intensity and can have a reversed contrast, which was not considered in [51]. In our qualitative model discussed above, the varying relative Kikuchi pattern contrast as a function of energy loss is addressed by the lengths λ_C and λ_A. These parameters can describe the decrease of the diffraction modulation relative to the mean intensity which is due to an increasing number of inelastic scattering events on the outgoing path.

Recently, for a convergent beam transmission geometry, Mendis studied Kikuchi contrast based on a multi-slice approach which incorporates changes in momentum due to plasmon excitation using Monte-Carlo techniques [52]. He concluded that the observed decrease in Kikuchi contrast after multiple plasmon excitation can be reproduced by changing the momentum of the fast electron after plasmon excitation by that of the excited plasmon. We observe here that the decrease in contrast as observed in figure 11 after n plasmon excitations along the outgoing path can indeed be reasonably well modelled by convoluting the original Kikuchi line n times with the corresponding broadening.

7. Conclusion

We have presented experimental measurements of Kikuchi band contrast as a function of energy loss in a systematically varying scattering geometry. As a general trend, we observe a reduction of diffraction contrast with increasing energy loss. This trend is also seen when comparing the glancing-in geometry with the glancing-out setting. In the latter case, a larger fraction of the inelastic scattering events is located on the outgoing path and the diffraction contrast is reduced faster as a function of energy loss. Our experimental data supports the interpretation that an increasing number of inelastic losses will reduce the observed Kikuchi pattern contrast, and that an increasing fraction of electrons contributes to the background with increasing energy loss.

The inelastic losses can be seen to influence the scattered electrons due to their momentum transfer, i.e. the detected direction of propagation is not the same as the one directly after the backscattering event. This causes a smoothing out of the contrast via the loss of coherence in the scattered waves. For large energy losses, we observe a trend to the reversal of the Kikuchi band contrast, which shows the influence of anomalous absorption of type-

1 Bloch waves by phonon excitation [35]. Especially at larger energy losses, corresponding to longer trajectories, the surviving contrast is a consequence of the intricate balance between these processes. In consequence, it is not straight-forward to predict under what conditions contrast reversal is expected for phosphor-screen based experiments, where one integrates over all energies. We have presented a simple model which allows to determine analytic distributions for the diffraction distances as a function of the scattering geometry and the energy loss. The model also allows to include the resulting decoherence effects due to inelastic scattering in a Kikuchi diffraction simulation. We have shown that the model reproduces the qualitative trends in our experimental observations.

Our observations indicate consequences for the possible treatment of diffraction effects in Monte Carlo simulations. As discussed above, the distribution of Kikuchi sources will be governed by λ^{quasi}, which is about an order magnitude larger than the total elastic mean free path. Concerning the Monte Carlo determination of the path length distribution which is relevant for Kikuchi diffraction, a 'last elastic scattering event'-approximation (see e.g. [53]) would thus lead to outgoing path lengths which are governed by the total elastic mean free path λ^{el} which are about order of magnitude shorter than λ^{quasi}. In this way, the 'last elastic scattering event'-approximation can lead to very short outgoing paths and result in a general blurring of diffraction features. Our results indicate that the last quasi-elastic incoherent scattering event on a trajectory should be considered as the origin of an incoherent Kikuchi source in MC simulations, in contrast to the last elastic event in general, which is more likely to be a small-angle, forward-scattering event contributing to the coherent diffraction effects. In MC simulations, for increasing path lengths and a correspondingly increasing number of inelastic losses, the role of multiple, angle-dependent plasmon scattering will become important. For example, the angle-dependence of multiple plasmon scattering is neglected in the continuous slowing down approximation, where energy losses do not change the direction of propagation in the Monte Carlo simulation.

In conclusion, we return to our initial question of why in EBSD we can observe Kikuchi pattern contrast under experimental conditions which involve multiple, elastic and inelastic, scattering processes but no explicit energy filtering. Kikuchi sources are created by quasi-elastic scattering processes, which involve the recoil of single atoms [5, 7]. This process provides the initial localization of the Kikuchi sources at the atomic sites in the unit cell, by which the Kikuchi pattern contributions from the atomic sites are favoured compared to the other positions in the unit cell. With reference to figure 2(a) this means that quasi-elastic incoherent events do not lead to an averaging out of contrast (see also [6]). For compound materials, energy-resolved measurements allow to disentangle these site-specific distributions via the recoil-energies of different atomic species [5, 7, 54]. Concerning the relative frequency of the events which create the incoherent Kikuchi sources, we have estimated in section 2 that the mean free path λ^{quasi} for the quasi-elastic scattering events is about an order of magnitude larger than the total elastic mean free path $\lambda^{\mathrm{el}}_{\mathrm{tot}}$ (table 1). At high energies, typical elastic scattering trajectories in the solid thus involve many more small-angle coherent forward scattering events than incoherent, larger angle scatterings. This is why we apply the v-type approximation [43] for the shape of the electron trajectories, in which a large-angle scattering event divides the total path in an incoming and outgoing part. Independent on the actual shape of the path, however, the average outgoing path after the last quasi-elastic scattering event will generally be of the order of λ^{quasi}.

While the approximate shape of the electron trajectories in the solid is essentially determined by the properties of the elastic cross sections [20], the energy distribution of the scattered electrons is determined by the energy loss function. From the model energy loss function for silicon which we presented in section 2.2, we calculated the inelastic mean free path λ^{in} in table 1. Because $\lambda^{\mathrm{quasi}} \gg \lambda^{\mathrm{in}}$, any part of a trajectory of the order of λ^{quasi} is likely to contain several inelastic events, i.e. it is relatively unlikely that the outgoing path after the last quasi-elastic event contains no inelastic events at all. Because inelastic scattering is known to destroy Kikuchi pattern contrast [10], a pronounced Kikuchi pattern contrast can thus be preserved only for a relatively low number of inelastic losses after the creation of a Kikuchi pattern source. This corresponds to a low total energy loss or to geometries which favour short outgoing paths, i.e. for glancing incidence of the electron beam.

Our experimental observations thus fully support the arguments given in [4] where it was demonstrated that a restricted spectral range is consistent with the observed Kikuchi contrast in EBSD patterns. Within the spectrum of backscattered electrons, diffraction effects are not a fixed fraction of the BSE signal at a given energy, but the backscattered electrons contribute increasingly to the background intensity with increasing energy loss. The qualitative model introduced in the present paper explains this experimental observation by the order-of-magnitude factor between the large mean free path length for quasi-elastic scattering as compared to the much shorter inelastic mean free path. Considering that the shape of high-energy electron trajectories is governed by elastic cross sections which change relatively slowly on the energy scale of inelastic losses [20], we can see that, near a given energy, an increasing number of loss events needs to take place on essentially the same type of trajectories, including the part of the trajectory after the last quasi-elastic event. Trajectories with a higher number of losses are thus also less likely to fulfill the conditions for effective Kikuchi diffraction, which requires that no or only a few further inelastic events occur after the last quasi-elastic event.

Acknowledgments

This work was supported by the Polish National Agency for Academic Exchange (NAWA), Grant No. PPN/ULM/2019/1/00068/U/00001.

ORCID iDs

M Vos https://orcid.org/0000-0003-2668-9216
A Winkelmann https://orcid.org/0000-0002-6534-693X

References

[1] Kikuchi S 1928 Diffraction of cathode rays by Mica *Proc. Imperial Acad.* **4** 354–6
[2] Reimer L, Heilers U and Saliger G 1986 Kikuchi band contrast in diffraction patterns recorded by transmitted and backscattered electrons *Scanning* **8** 101
[3] Williams D B and Carter C B 2009 Kikuchi diffraction *Transmission Electron Microscopy* (Berlin: Springer) pp 311–22
[4] Winkelmann A, Britton T B and Nolze G 2019 Constraints on the effective electron energy spectrum in backscatter Kikuchi diffraction *Phys. Rev.* B **99** 064115
[5] Winkelmann A and Vos M 2011 Site-specific recoil diffraction of backscattered electrons in crystals *Phys. Rev. Lett.* **106** 085503
[6] Winkelmann A and Vos M 2013 The role of localized recoil in the formation of Kikuchi patterns *Ultramicroscopy* **125** 66–71
[7] Vos M, Winkelmann A and Nolze G 2015 Element-specific Kikuchi patterns of rutile *Ultramicroscopy* **156** 50
[8] Komuro M, Kojima S and Ichinokawa T 1972 Contrast reversal of Kikuchi bands in transmission electron diffraction *J. Phys. Soc. Japan.* **33** 1415
[9] Reimer L 1979 Electron diffraction methods in TEM, STEM and SEM *Scanning* **2** 3
[10] Winkelmann A and Nolze G 2010 Analysis of Kikuchi band contrast reversal in electron backscatter diffraction patterns of silicon *Ultramicroscopy* **110** 190
[11] Salvat F 2003 Optical-model potential for electron and positron elastic scatteing by atoms *Phys. Rev.* A **68** 012708
[12] Went M, Vos M and Elliman R G 2007 Electron inelastic mean free path in solids as determined by electron Rutherford back-scattering *J. Electron Spectrosc. Relat. Phenom.* **156–158** 387–92
[13] Müller H, Rose H and Schorsch P 1998 A coherence function approach to image simulation *J. Microsc.* **190** 73–88
[14] Flensburg C and Stewart R F 1999 Lattice dynamical Debye–Waller factor for silicon *Phys. Rev.* B **60** 284
[15] Wang Z L 2003 Thermal diffuse scattering in sub-angstrom quantitative electron microscopy–phenomenon, effects and approaches *Micron* **34** 141
[16] Rossouw C J and Bursill L A 1986 Dynamical thermal diffuse scattering of fast electrons in rutile *Proc. R. Soc.* A **408** 149
[17] Egerton R F 2011 *Electron Energy-Loss Spectroscopy in the Electron Microscope* 3rd edn (New York: Plenum Press)
[18] Shinotsuka H, Tanuma S, Powell C J and Penn D R 2015 Calculations of electron inelastic mean free paths. X. Data for 41 elemental solids over the 50 eV to 200 keV range with the relativistic full Penn algorithm *Surf. Interface Anal.* **47** 871
[19] Ding Z-J and Shimizu R 1996 A Monte Carlo modeling of electron interaction with solids including cascade secondary electron production *Scanning* **18** 92–113
[20] Werner W S M 2001 Electron transport in solids for quantitative surface analysis *Surf. Interface Anal.* **31** 141
[21] Stobbs W and Bourdillon A 1982 Current applications of electron energy loss spectroscopy *Ultramicroscopy* **9** 303
[22] Allen L J and Josefsson T W 1995 Inelastic scattering of fast electrons by crystals *Phys. Rev.* B **52** 3184
[23] Jin H, Shinotsuka H, Yoshikawa H, Iwai H, Tanuma S and Tougaard S 2010 Measurement of optical constants of Si and SiO_2 from reflection electron energy loss spectra using factor analysis method *J. Appl. Phys.* **107** 083709
[24] Henke B, Gullikson E and Davis J 1993 X-ray interactions: photoabsorption, scattering, transmission, and reflection at $E = 50$–30,000 eV, $Z = 1$–92 *At. Data Nucl. Data Tables* **54** 181
[25] Vos M and Grande P L 2019 Modeling the contribution of semi-core electrons to the dielectric function *J. Phys. Chem. Solids* **124** 242
[26] Pines D 1963 *Elementary excitations in solids* (New York: Benjamin)
[27] Kamiya Y and Uyeda R 1961 Effect of incoherent waves on the electron microscopic images of crystals *J. Phys. Soc. Japan.* **16** 1361
[28] Howie A 1963 Inelastic scattering of electrons by crystals I. The theory of small-angle inelastic scattering *Proc. R. Soc.* A **271** 268
[29] Howie A 2011 Mechanisms of decoherence in electron microscopy *Ultramicroscopy* **111** 761
[30] Dudarev S, Peng L-M and Whelan M 1992 On the damping of coherence in the small-angle inelastic scattering of high-energy electrons by crystals *Phys. Lett.* A **170** 111
[31] Winkelmann A, Trager-Cowan C, Sweeney F, Day A P and Parbrook P 2007 Many-beam dynamical simulation of electron backscatter diffraction patterns *Ultramicroscopy* **107** 414–21
[32] Winkelmann A 2009 Dynamical simulation of electron backscatter diffraction patterns *Electron Backscatter Diffraction in Materials Science* ed A J Schwartz *et al* (Berlin: Springer) ch 2 (https://doi.org/10.1007/978-0-387-88136-2_2)
[33] Kainuma Y 1955 The theory of Kikuchi patterns *Acta Crystallogr.* **8** 247
[34] Laue M v 1948 *Materiewellen und ihre Interferenzen* (Berlin: Akademische Verlagsgesellschaft Leipzig)
[35] Humphreys C J 1979 The scattering of fast electrons by crystals *Rep. Prog. Phys.* **42** 1825–87
[36] Winkelmann A 2009 Principles of depth-resolved Kikuchi pattern simulation for electron backscatter diffraction *J. Microsc.* **239** 32
[37] Brodu E, Bouzy E and Fundenberger J-J 2017 Diffraction contrast dependence on sample thickness and incident energy in on-axis Transmission Kikuchi Diffraction in SEM *Ultramicroscopy* **181** 123
[38] Matsui F, Matsushita T, Hashimoto M, Goto K, Maejima N, Matsui H, Kato Y and Daimon H 2012 Negative photoelectron diffraction replica in secondary electron angular distribution *J. Phys. Soc. Japan.* **81** 013601
[39] Winkelmann A 2014 Influence of localized inelastic scattering on Kikuchi bands in photoelectron diffraction patterns *J. Electron. Spectrosc. Relat. Phenom.* **195** 361
[40] Vos M, Cornish G P and Weigold E 2000 A high-energy (e,2e) spectrometer for the study of the spectral momentum density of materials *Rev. Sci. Instrum.* **71** 3831–40
[41] Vos M and Winkelmann A 2016 Two-dimensional Kikuchi patterns as measured using an electrostatic analyser *Ultramicroscopy* **171** 19

[42] Dubus A, Jablonski A and Tougaard S 2000 Evaluation of theoretical models for elastic electron backscattering from surfaces *Prog. Surf. Sci.* **63** 135–75
[43] Yubero F, Pauly N, Dubus A and Tougaard S 2008 Test of validity of the {V-type} approach for electron trajectories in reflection electron energy loss spectroscopy *Phys. Rev.* B **77** 245405
[44] Hall C R and Hirsch P B 1965 Effect of thermal diffuse scattering on propagation of high energy electrons through crystals *Proc. R. Soc.* A **286** 158–77
[45] Zuo J M and Spence J C H 2017 *Advanced Transmission Electron Microscopy* (Berlin: Springer) (https://doi.org/10.1007/978-1-4939-6607-3)
[46] Winkelmann A, Aizel K and Vos M 2010 Electron energy loss and diffraction of backscattered electrons from silicon *New J. Phys.* **12** 053001
[47] Boersch H 1953 Gegenfeldfilter für Elektronenbeugung und Elektronenmikroskopie *Z. Phys.* **134** 156
[48] Deal A, Hooghan T and Eades A 2008 Energy-filtered electron backscatter diffraction *Ultramicroscopy* **108** 116–25
[49] Berger M, Coursey J, Zucker M and Chang J Stopping-power & range tables for electrons, protons, and helium ions NIST Standard Reference Database (https://doi.org/0.18434/T4NC7P)
[50] Moore K, Howe J and Elbert D 1999 Analysis of diffraction contrast as a function of energy loss in energy-filtered transmission electron microscope imaging *Ultramicroscopy* **80** 203
[51] Ram F and Graef M D 2018 Energy dependence of the spatial distribution of inelastically scattered electrons in backscatter electron diffraction *Phys. Rev.* B **97** 134104
[52] Mendis B 2019 An inelastic multislice simulation method incorporating plasmon energy losses *Ultramicroscopy* **206** 112816
[53] Callahan P G and Graef M De 2013 Dynamical electron backscatter diffraction patterns. I: pattern simulations *Microsc. Microanal.* **19** 1255–65
[54] Vos M and Winkelmann A 2017 Element-resolved Kikuchi pattern measurements of non-centrosymmetric materials *Mater. Charact.* **123** 328–38